



Investigation of mesoporous carbon hollow spheres as catalyst support in DMFC cathode

T. Tesfu-Zeru, M. Sakthivel, J.-F. Drillet*

DECHEMA-Forschungsinstitut, Theodor-Heuss-Allee 25, 60486 Frankfurt am Main, Germany



ARTICLE INFO

Article history:

Received 3 July 2016

Received in revised form 2 November 2016

Accepted 8 November 2016

Available online 9 November 2016

Keywords:

Pt catalyst

Mesoporous Hollow Graphitic Spheres (HGS)

Middle-temperature DMFC

Accelerated degradation tests (ADT)

ABSTRACT

In conventional low temperature PEM fuel cells, catalyst activity and stability rely on adequate structure and morphology of carbon support material, especially at the cathode that is exposed to high potential values. Degree of graphitization as well as pore distribution are decisive parameters for corrosion resistivity, catalyst utilization and mass transport. In this work, hollow graphitized carbon spheres (HGS) with mesoporous structure were tested as catalyst support in middle temperature (90–110 °C) direct methanol fuel cell (DMFC) cathode. Influence of catalyst loading and concentration as well as working temperature on power density was studied in a 5 cm² laboratory cell. Best results in terms of MEA performance were achieved with a catalyst loading of 2 mg_{Pt} cm⁻² at both electrodes and an extremely dense Pt concentration on carbon support of 50 and 40 wt% at the anode and cathode, respectively at 110 °C. Additionally, thermal pretreatment of carbon-supported catalyst up to 850 °C led to increase in particle size up to 7 nm and as a consequence to substantial higher ECSA retention during accelerated degradation test (ADT) under half-cell conditions.

© 2016 Elsevier B.V. All rights reserved.

1. Introduction

Finding sustainable solutions to face increasing energy demand, reducing our dependence on fossil resources and limiting environmental impacts such as global warming of industrial activities are some urgent challenges to overcome [1,2]. Hydrogen-based fuel cells are attractive decentralised alternative power sources for automotive [3], portable and stationary applications especially as heat and electricity plant for domestic applications [4,5] since it is capable of supplying high power densities with high efficiency under rapid load fluctuation. Fuel cells directly convert chemical energy of fossil-based fuels such as H₂ [6], CH₃COH [7] and CH₄ [8] into electrical energy.

In case of the low temperature PEMFC, the so-called membrane-electrodes assembly (MEA) is composed of a proton-conducting polymer membrane (e.g. Nafion) and two gas diffusion electrodes (GDE). Depending on the coating strategy and more precisely on desired layer thickness, active material can be applied either directly on the membrane or on the gas diffusion layer (GDL) to form a catalyst coated membrane (CCM) or a catalyst coated electrode (CCE), respectively. In order to improve gas distribution and

mass transport of the reaction educts and products, especially at the cathode where water flooding is a concern, a microporous layer (MPL) consisting of carbon black is commonly deposited on macro-porous GDL [9]. The latter is generally made of woven or non-woven carbon fibre matrix and is known as carbon cloth or carbon paper, respectively with typically 75–85% void volume.

GDEs are subjected to several partially competitively technical challenges and have permanently to be optimized in terms of fuel and reaction products distribution, water management, electronic conductivity as current collector, heat transfer and mechanical strength compound for polymer electrolyte structure in combination with flow field as well as corrosion resistance [10]. Recently, See et al. [11] investigated effect of the GDL material on thermal behavior along reactant flow channels in PEMFCs by using confocal laser scanning microscopy. They found that particularly in-plane thermal conductivity and morphological structure play an important role with respect to temperature gradient and water distribution in flow channels. Recent developments on single- and dual-layered GDL on reactant diffusion and water management in PEM fuel are reviewed in Park et al. [12].

The reaction layer is commonly made of a mixture of Pt-based nanoparticle dispersed on high surface carbon black support and a binder material such as Nafion/PTFE. One essential prerequisite for high cell performance is related to formation of the so-called triple-phase-boundary that should allow perfect juxtaposition of

* Corresponding author.

E-mail address: drillet@dechema.de (J.-F. Drillet).

liquid, gas and solid phases and therefore good accessibility of gas molecules to the active catalyst sites [1,13]. Numerous works have focused on development of more performing catalyst materials like alloying/dealloying Pt-based catalysts [14], bimetallic core/shell nanoparticles [15] and nanostructured thin-film catalysts for oxygen reduction reaction (ORR). However, up to now, most of them still show challenging instability issues due to coalescence, ripening and dissolution of the active catalyst as well as support corrosion that shorten their practical lifetime [16].

One attractive strategy to get higher cell performance consists on elevating cell temperature. That results in higher reaction and mass transfer rates, and usually in lower cell resistance arising from higher ionic conductivity of the polymer electrolyte. The latter strongly depends on proton mobility within polymer pathway [17]. Another profitable advantage of higher temperature level is related to enhancement of the electro-catalyst CO tolerance in cells running on reformate fuel [18]. An increase in operating pressure generally leads to higher partial pressure of reactant gases, solubility, and mass transfer rates and consequently to higher cell efficiency as noted by Angrist et al. [19].

Mass transport resistance is depending on several inherent parameters such as electrode porosity, capillarity effect, hydrophobicity level, compression force of end plates, and geometry of low field channels and is more pronounced at high current density values where high diffusion rate of reactants and products to/from reaction sites are required to avoid electrode flooding. Bogolowski et al. [20] demonstrated that combination of both high current densities with low methanol concentration can lead to methanol yield efficiencies higher than 85%. Ideally, methanol concentration at the membrane/anode interface should tend to zero.

In this context, properties of the catalyst support are of great importance. It is meanwhile well-known, that adequate mesoporous structure with pore size in the range of catalyst particle favors catalyst stability and durability. Combination of ideal pore size distribution in the range of 2 nm and high electrical conductivity of mesoporous CMK-3 support was found to enhance Pt activity for electrochemical methanol oxidation [21]. One distinguishes ordered (OMC) from disordered mesoporous (DOMC) carbon ones, which can be prepared either by using e.g. silica templates e.g. SBA-15 [22] or triblock copolymer template structures [23,24]. It should be noted that hereby choice of the synthesis route (hard or soft template) may also influence electrochemical cell performance [25]. Nowadays these materials are widely studied for their application in Li-ion batteries and fuel cells as catalyst support materials [26–29]. Oxygen-functionalized mesoporous carbon surface can improve interaction between metal catalyst and carbon support by promoting uniform dispersion. It is stated that surface chemistry plays an important role in porous materials and predefined monodispersed pore morphology enables easier mass transportation which is much more prominent in case of liquid reaction [30]. It was also observed that ohmic and mass transfer polarization losses were more significant for highly functionalised support samples. This was attributed to decreased electrical conductivity, higher agglomeration and lower specific surface area [31,32].

Influence of the pore volume and ionomer content in reaction layer on cell performance was addressed in [32]. The influence of mesoporous carbons as support for bi-metallic catalyst systems was investigated in [31,33]. Because of their high surface area, large pore volume and narrow pore size distribution, more homogeneous dispersion and better accessibility of bi-metallic catalyst was obtained that favoured higher catalyst utilization during the electrochemical reaction in fuel cells and may allow a reduction of both loading and cost. Alloys of Pt with other non-precious metals such as Fe, Co, and FeCo have also been studied on mesoporous carbon support [34]. Therein, polarization tests with cyclic voltammetry revealed that kinetic current density of the bi-metal

catalyst on mesoporous support at 0.9 V amounted 1.80 mA cm^{-2} and surpassed by 80% that measured at the Pt/Vulcan catalyst (1.00 mA cm^{-2}).

Activity of nitrogen-doped mesoporous carbon for ORR was evaluated in [35,36]. Hereby a very narrow pore-size distribution of ca. 3.8 nm was obtained. By using a aqueous hydrothermal route at 70 °C, mesoporous carbon support with small nitrogen content (<1%) provided a large surface area and a graphitic framework, leading to high electrocatalytic activity, excellent long term stability, and high resistance to methanol crossover effects for the ORR compared to commercial Pt/Vulcan as stated in [37].

The main aim of this work focuses on the decoration of hollow spherical carbon with nano-dispersed Pt and their test as cathode material in DMFC.

2. Experimental

All purchased chemicals had analytical grade quality and were used without any further purification. Hollow Graphitic Spheres (HGS, ca. 280–400 nm in diameter) were provided by Max-Planck Institute for Carbon Research in Mülheim an der Ruhr in Germany and synthesized by using a silica exotemplate route as described elsewhere [38]. Benchmark Carbon Vulcan (XC72R, Cabot Corp.) was used as reference in this work. Pt/C catalyst was prepared by impregnating carbon support with desired amount of hexachloroplatinic acid ($\text{H}_2\text{PtCl}_6 \cdot 6\text{H}_2\text{O}$, 99.99%, Alfa Aesar GmbH) followed by reduction process in 37 wt% formaldehyde stabilized with 10% methanol (Merck KGaA) at 80 °C for 1 h under reflux conditions. Reaction products were washed with ultrapure water ($>18.18 \text{ M}\Omega \text{ cm}$, ELGA, Millipore), filtered through a 0.45 μm polycarbonate membrane (Sartorius AG) and finally dried at 80 °C in a vacuum furnace (VT6025, Thermo Fisher Scientific Inc.) at 50 mbar for 4 h. Post-thermal treatment of the as-prepared Pt/Vulcan and Pt/HGS was carried out at 850 °C under N_2 atmosphere at 850 °C for 2 h. For the anode, a 40 wt% (1:1) Pt-Ru/HSAG catalyst was purchased by Alfa Aesar (HiSPEC™ 12100). Typical GDE fabrication procedure was carried out as follows: 500 mg carbon-supported catalyst, 20 wt% PTFE and 10 wt% Nafion were suspended in a 1:2 water:isopropanol (Carl Roth GmbH) solvent mixture, stirred for 30 min and then sprayed with an ultrasonic-supported coating machine (Prism-450, Ultrasonic Systems, Inc.) onto either a gas diffusion layer (GDL) with microporous layer (MPL) (CH2315CX190, Freudenberg & Co.) for the cathode or onto a blank carbon paper (TGP-H-60, Toray Industries, Inc.) for the anode until reaching desired catalyst loading value. Finally, as-coated GDE were sintered in an oven at 80 °C for 1 h. Afterwards, membrane electrode assembly (MEAs) was fabricated by hot-pressing (Labopress 200S, Vogt GmbH) the 5 cm^2 GDE cathode and anode with a Nafion® 117 membrane (QuinTech GmbH) at 130 °C and 7 bar for 4 min, that was previously protonated by successive boiling steps in 1 M H_2SO_4 , 3% H_2O_2 and H_2O for 1 h, respectively.

Electrochemical half cell investigations were performed with a 0.5 cm^2 rotating glassy carbon disk electrode (RDE) (Jaissle Elektronik GmbH). For sample preparation, 2 mg of carbon-supported catalyst was first dispersed in a 1 ml water:isopropanol mixture (1:2) and ultrasonicated for 5 min. Then 0.2 mg (10 wt%) of Nafion® (Ion Power, Inc.) was added and the suspension and stirred for 30 min. About 20 μl of the ink was transferred onto the glassy carbon electrode and dried in vacuum oven at 50 °C for 1 h. A total catalyst loading of about $80 \pm 10 \text{ } \mu\text{g}_{\text{Pt}} \text{ cm}^{-2}$ was obtained for all systems. It was determined by depositing identical volume of catalyst ink on Au disk electrode of an electrochemical quartz balance (6 MHz; PGSTAT302 N, Metrohm Autolab B.V.). Prior to each experiment, glassy carbon surface was cleaned with isopropanol, polished with a 0.05 μm alumina suspension and finally dried at 80 °C for 1 h.

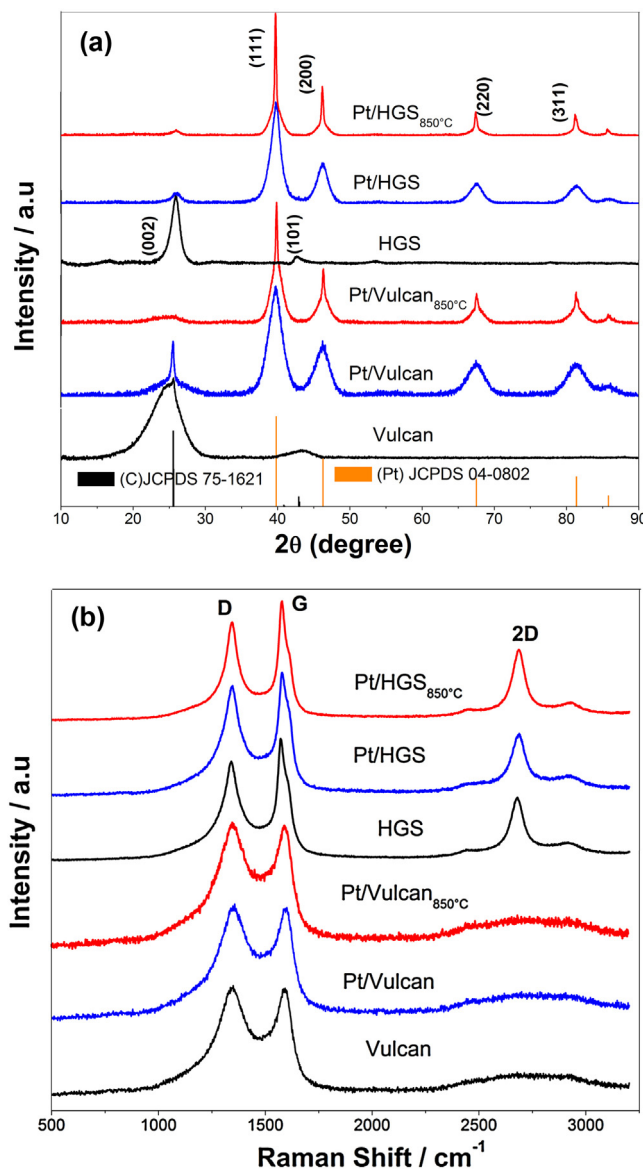


Fig. 1. (a) XRD patterns and (b) Raman spectra of Vulcan, HGS carbons, Pt/Vulcan and Pt/HGS catalysts.

Steady-state cyclic voltammograms (CV) were recorded with a bi-potentiostat (PG 100, Jaissle Elektronik GmbH). A Pt wire and a saturated calomel electrode (SCE, +244 mV vs. NHE) were employed as counter and reference electrode, respectively. Electrochemical surface area (ECSA) of the catalyst was calculated by integrating hydrogen desorption region between 0.005 and 0.36 V vs. NHE in the CV at 40 mV s⁻¹ and by assuming that the charge induced by a monolayer of hydrogen atoms on Pt amounts 210 μC cm⁻². Oxygen reduction reaction (ORR) measurements were performed in an oxygen-saturated 0.5 M H₂SO₄ and 0.5 M CH₃OH containing 0.5 M H₂SO₄ electrolyte at 1600 rpm and cathodic sweep of 5 mV s⁻¹. Accelerated degradation tests (ADT) were carried out in a N₂-saturated electrolyte and consisted of 7000 cycles in potential range of 0.4–1.4 V at dE/dt = 1000 mV s⁻¹. All potentials mentioned in this work are normalized to the normal hydrogen electrode (NHE). DMFC investigations were performed in a 5 cm² commercial single cell (ElectroChem, Inc.) designed with combination of serpentine/parallel graphite flow fields and with gold-coated copper end plates. Flow rate was set to 10, 200 and 700 ml min⁻¹ for methanol, oxygen and air, respectively. The methanol was forced

through the DMFC by a pump (ISM321A, Ismatec) and pressurized by a pressure controller at the desired value (5866, Brooks) as shown in Fig. S1 in supplement information (SI). Cell performance was evaluated by means of U-I polarization measurements with an electronic load (DS800, Höcherl & Hackl GmbH).

Structural composition of the catalysts was analysed by X-ray diffractometer (XRD) (D8 Advance, Bruker GmbH) equipped with Cu-K_α radiation ($\lambda = 0.154$ nm). The crystalline structure of carbon was studied by Raman spectroscopy (inVia, Renishaw plc.) equipped with a confocal microprobe optics. An Ar-ion laser beam with wavelength of 532 nm was used as the excitation source and focused through a 50 x magnification lens and reached about a 1 μm spot size on sample surface. The laser power was fixed to 1% of maximum power source (100 mW). Raman instrument is coupled to an optical microscope (DM 2500, Leica Camera AG). Each measurement was carried out within the spectral range between 100 and 3200 cm⁻¹ with the nominal spectral resolution of 1 cm⁻¹ at room temperature. A high resolution diffraction grating density of 1800 grooves mm⁻¹ was applied to disperse the Stokes-scattered radiation at the CCD camera (RenCam CCD detector, 1024 × 256 pixels) thermoelectrically cooled at -70 °C. The recorded spectra consist of 20 overlayed scans with an acquisition time of 20 s each. The background of all spectra was subtracted according to the baseline correction mode. The samples were analysed without any additional sample treatment or preparation. Thermal decomposition behavior of carbon and Pt metal loading was estimated by thermogravimetric analysis (TGA) (STA 449C, Netzsch GmbH) at MPI in Mülheim by increasing the temperature from 25 °C to 1000 °C with a heating rate of 20 °C min⁻¹ in air flow of ca. 60 ml min⁻¹. Surface morphology, electrode thickness and atomic/weight ratio of the catalysts were examined by scanning electron microscope (SEM) and energy dispersive X-ray spectroscopy (EDX) (XL 40, Philips N. V.), respectively. Transmission electron microscope (TEM) images were taken at an acceleration voltage of 120 kV (EM420, Philips N. V.). Element maps with a spatial resolution of about 1 μm were obtained by electron probe microanalysis (EPMA) (JXA 8100, JEOL Ltd.) applying wavelength-dispersive X-ray spectroscopy (WDX).

3. Results and discussion

3.1. Influence of heat treatment on particle size

Fig. 1a shows X-ray diffraction (XRD) patterns of carbon Vulcan and HGS as well as of Pt/Vulcan and Pt/HGS before and after thermal treatment in N₂ at 850 °C with their corresponding standards. From the shape of first peak at 26.23° in pure carbon spectra, it can be deduced that HGS has more crystalline/graphitic domains than Vulcan. Interestingly, after Pt deposition, peak ratio (111/002) is lower in case of Pt/Vulcan sample. Since no change is visible in Raman spectrum after Pt deposition and temperature treatment (see **Fig. 1b**), the decrease in intensity of (002) peak in Pt/HGS spectra results obviously from higher Pt density on surface support compared to Vulcan-based systems (see TEM images in **Fig. 2**

a-d). The diffraction peaks of Pt/Vulcan and Pt/HGS are well indexed to the (111), (200), (220), (311) planes in JCPDS card 04-0802. Both catalyst systems were identified as a face centered cubic (fcc) structure. After temperature treatment at 850 °C, peak morphology of both catalyst is becoming sharper. This is related to particle growth due to particle diffusion/coalescence on support material. Average particle size of Pt/Vulcan, Pt/Vulcan_{850 °C}, Pt/HGS, and Pt/HGS_{850 °C} systems was calculated by applying Scherrer formula [39] to (111) peak and amounted 3.67, 6.45, 5.31 and 7.9 nm, respectively that represents a growth of 76% for Pt/Vulcan and 49% for Pt/HGS.

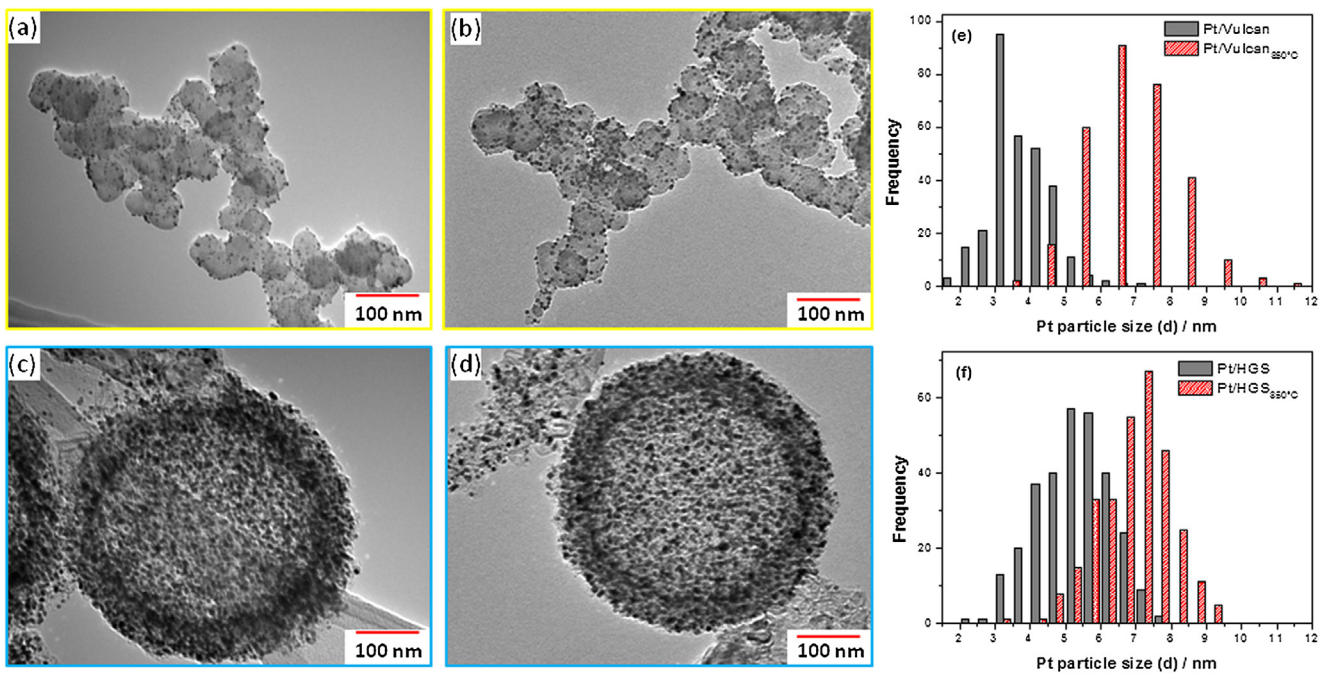


Fig. 2. TEM images of 33 wt% Pt catalysts (a and c) before and (b and d) after thermal treatment at 850 °C with (e and f) corresponding histograms of particle sizes distribution.

Fig. 1b shows Raman spectra of both pure carbons and carbon-supported Pt catalysts in which well-resolved D (defect), and G (graphitic) bands at around 1350 cm⁻¹ and 1580 cm⁻¹ that corresponds to tangential vibration of the carbon were detected. Alteration of carbon nature caused by Pt deposition and temperature treatment is not visible. Higher G/D ratio and presence of 2D peak at 2694 cm⁻¹ in case of HGS-based systems are indications for higher graphitic domains compared to Vulcan-based ones. The amount of Pt metal loading on all Vulcan and HGS carbon systems was evaluated to 33 wt% from TGA measurements after carbon oxidation at 1000 °C in air.

Fig. 2 shows typical TEM images of the 33 wt% Pt/C and 33 wt% Pt/HGS (a, c) before and (b, d) after thermal treatment as well as corresponding histograms related to Pt particle size distribution based on optical observation of more than 300 particles. Average size of as-prepared Pt was estimated to approximately 3.6, 6.8, 5.3 and 7.0 nm for Pt/Vulcan, Pt/Vulcan_{850 °C}, Pt/HGS and Pt/HGS_{850 °C} catalysts, respectively. The size of Pt particles evaluated from the TEM images are in consistence with that calculated from the XRD peak broadening. Size and shape of Pt particles depend on nature of the pores in carbon support and presence of anchoring sites such as functional groups [40]. It is well known that conventional carbon Vulcan contains mesoporous (2–50 nm) and microporous (<2 nm) bimodal pore system [41], whereas micropore domains are generally not accessible during catalyst deposition and consequently don't participate to reaction process. By contrast, HGS with major pore size volume in the range of 3–4 nm and minor fraction with sizes of about 8–10 nm [38] is more appropriate as support material. In addition, HGS material possesses a three-dimensional interconnected mesopore system that may host high concentration of Pt particles as can be seen in **Fig. 2c** and **2d**.

After post thermal treatment, a decrease in density and increase in particle size of Pt on both Vulcan and HGS supports is visible on corresponding TEM image whereas Pt particle growth on Vulcan is relatively higher ($\times 1.88$) than that observed on HGS support ($\times 1.32$). This is attributed to easier migration and aggregation of smaller particles on Vulcan surface, which is additionally favoured by temperature close to so-called Tammann value [42] of

884 °C = $T_{\text{Pt,melting}}/2$. In contrast, HGS mesoporous structure offer ideal particle confinement that acts as efficient barrier against catalyst migration/coalescence/ripening processes. The average diameter of Vulcan and HGS single particle was evaluated to about 50 and 340 nm, respectively.

3.2. Evaluation of methanol tolerance of Pt/HGS during ORR under half-cell condition

The activity of Pt catalysts for the oxygen reduction reaction (ORR) was determined in oxygen-saturated electrolyte with the rotating disc electrode (RDE) under forced convection conditions at 100–2500 rpm. For better clarity, only measurements performed at 1600 rpm are presented in **Fig. 3a**. In pure H₂SO₄ electrolyte, all the investigated catalyst systems exhibit kinetic-, mixed kinetic/diffusion- and pure diffusion-controlled behavior. In the kinetic-controlled region between 750 and 850 mV, HGS-supported systems exhibit faster kinetics than Vulcan-based catalysts. It appears that thermal treatment of Pt/Vulcan_{850 °C} and Pt/HGS_{850 °C} caused a marginal shift of polarization potential for ORR of about 4 and 16 mV at 3 mA cm⁻² to more negative value, respectively. This is obviously due to an increase in Pt particle size. In potential region between 700 and 800 V, a quite abrupt transition from kinetics-controlled to diffusion-controlled regime is visible at HGS-based catalysts that may be an indication for optimal morphology of the hollow spheres and as a consequence for better accessibility of catalyst active sites compared to the chain-like Vulcan structure.

The influence of 0.5 M CH₃OH on catalyst activity towards ORR is shown in **Fig. 3b**. It is manifest that the large anodic peak observed at 0.675 V during cathodic scan of Pt/Vulcan catalysts can be ascribed to its large affinity for methanol oxidation reaction (MOR). In contrast, Pt/HGS catalysts exhibit a higher selectivity for the ORR and consequently lower mixed-potential values in the 500–700 mV potential window compared to Pt/Vulcan. Whether this effect can be attributed to adsorbed functional groups on HGS surface during preparation is still unclear. This will be studied more into details in a future work.

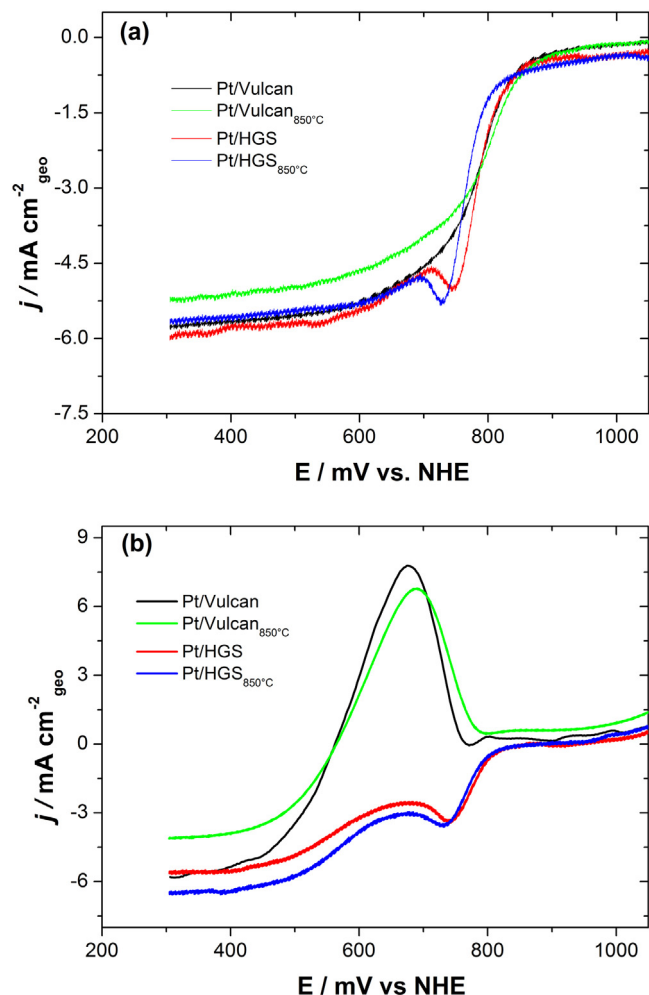


Fig. 3. ORR polarization curves of the Pt/Vulcan and Pt/HGS catalysts in O_2 -saturated (a) 0.5 M H_2SO_4 and in (b) 0.5 M CH_3OH containing 0.5 M H_2SO_4 electrolyte at 5 mV s^{-1} , 1600 rpm and 25 °C.

3.3. ADT under half-cell condition

Fig. 4a and b shows electrochemical CV characteristics of both as-prepared and thermally treated Pt/Vulcan and Pt/HGS catalysts before and after ADT test. Both catalysts exhibit typical hydrogen adsorption/desorption, double layer and oxide formation/reduction regions for polycrystalline Pt. The inset in Fig. 4a shows the baseline for charge evaluation of hydrogen desorption region used for ECSA calculation. Pt/HGS catalyst exhibited highest both ECSA and double layer capacity values that result from higher accessibility of Pt particles for proton species and largest specific BET area ($1200 \text{ m}^2 \text{ g}^{-1}$) of the HGS support compared to Vulcan

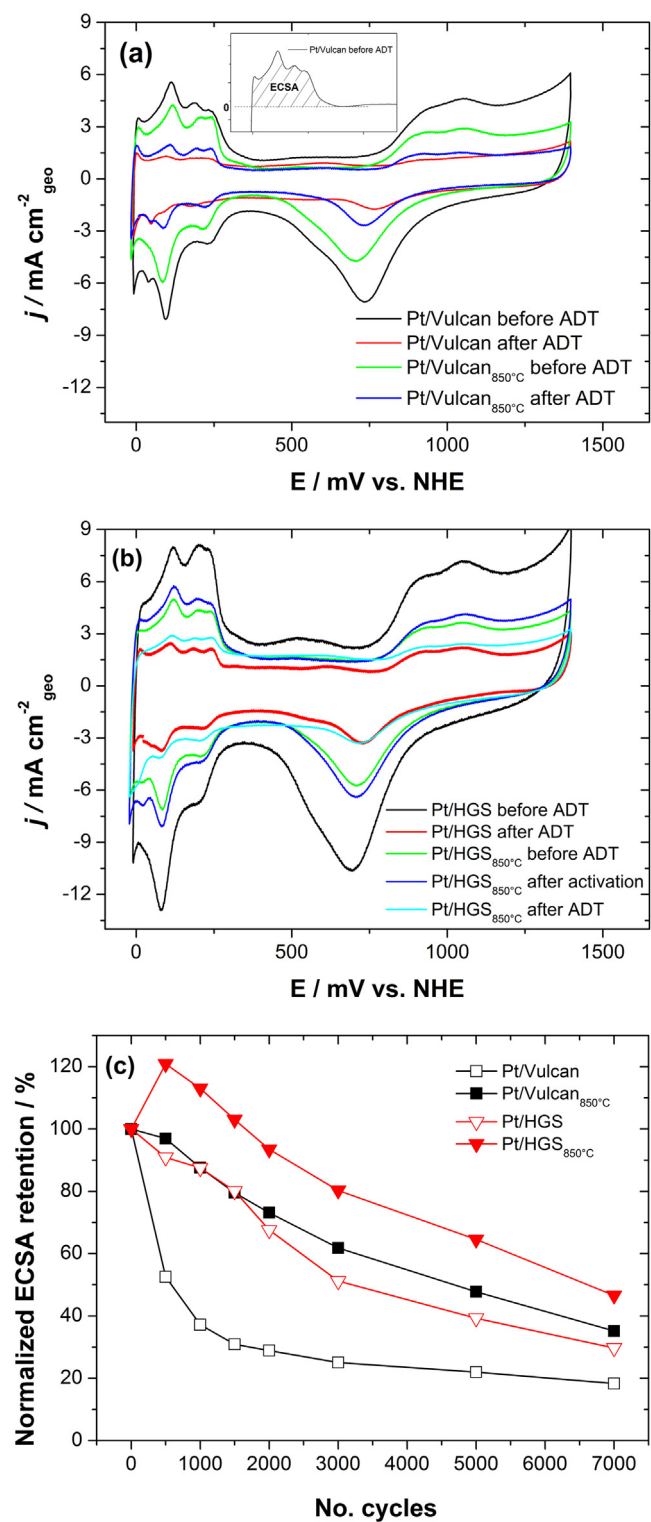


Table 1
Evolution of ECSA values of the different Pt/C during ADT test.

No. Cycles	ECSA/cm ²			
	Pt/Vulcan	$\text{Pt/Vulcan}_{850^\circ\text{C}}$	Pt/HGS	$\text{Pt/HGS}_{850^\circ\text{C}}$
1	52.97	45.49	111.62	41.55
500	27.84	44.09	101.47	50.23
1000	19.71	39.84	97.69	46.95
1500	16.38	36.18	89.43	42.82
2000	15.31	33.26	75.45	38.85
3000	13.26	28.13	57.19	33.36
5000	11.65	21.72	43.87	26.84
7000	9.71	16.0	33.2	19.36

Fig. 4. CVs of as-prepared and thermally treated 33 wt% (a) Pt/Vulcan and (b) Pt/HGS catalysts before and after 7000 ADT cycles in 0.5 M H_2SO_4 between 0 and 1.4 V at 1 V s^{-1} and 25 °C. (c) Evaluation of electrochemical surface area (ECSA) retention of Pt/Vulcan and Pt/HGS during ADT cycling.

system ($240 \text{ m}^2 \text{ g}^{-1}$), respectively. Surprisingly, after post-thermal treatment at 850°C , large decrease in ECSA, especially for Pt/HGS system (60% compared to 14% for Pt/Vulcan), is obvious that do not correlate with increase in particle size observed on TEM images (from $d_{\text{avg}} = 5\text{--}7 \text{ nm}$ for Pt/HGS compared to 3–8 nm for Pt/Vulcan). This can be attributed to a pore obstruction by HGS carbon structure

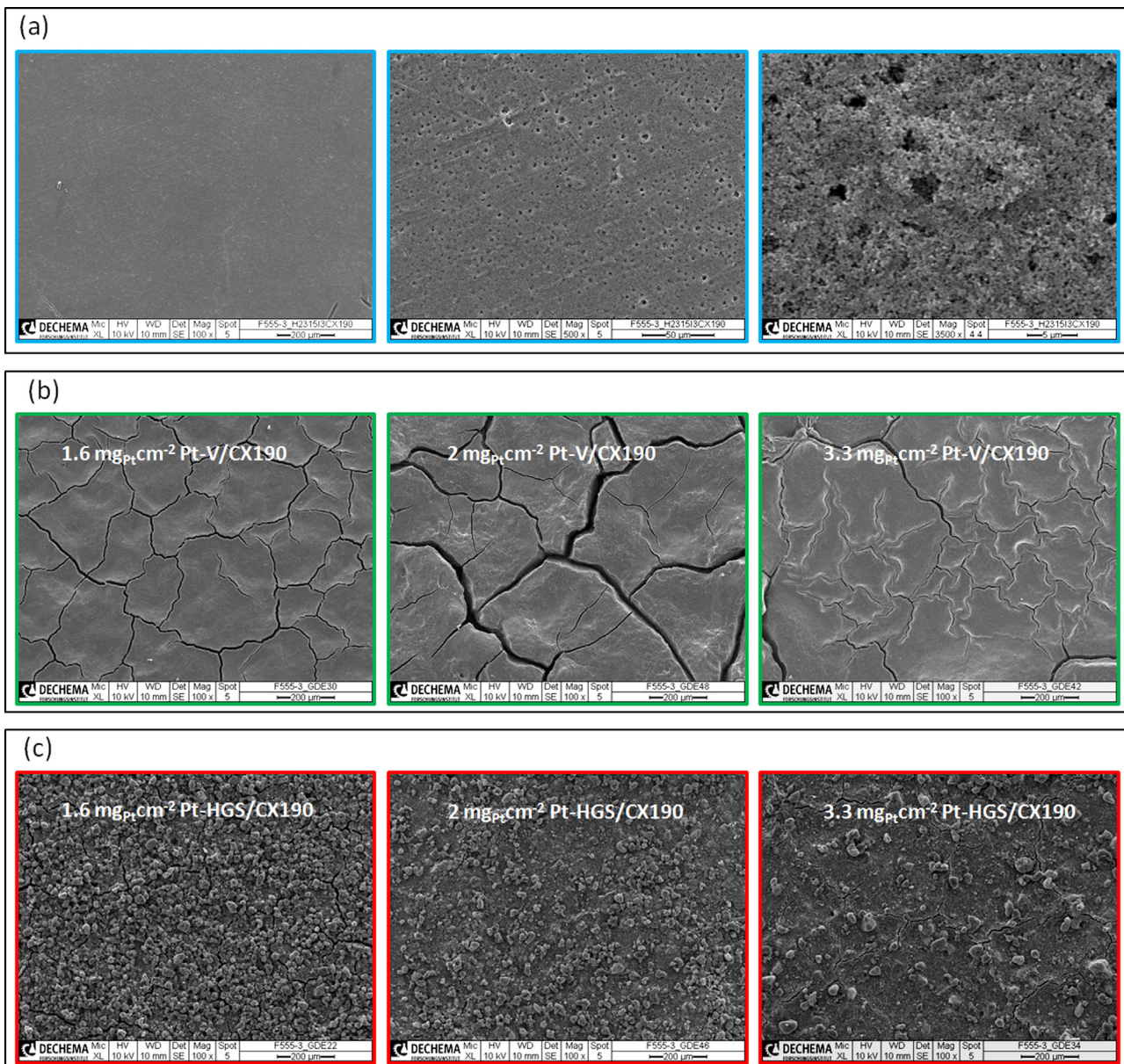


Fig. 5. SEM images of (a) MPL only (H2315I3 CX190) at different magnifications, (b) Pt/Vulcan and (c) Pt/HGS surfaces with increasing Pt catalyst loading: (left) 1.6 mg_{Pt} cm⁻², (middle) 2 mg_{Pt} cm⁻² and (right) 3.3 mg_{Pt} cm⁻².

decomposition during thermal treatment that reduces electrolyte accessibility to Pt active sites.

Fig. 4c resumes normalized ECSA behavior of different systems with respect to ADT cycle number while absolute values are listed in Table 1. After first 500 cycles, all ECSA values decreases continuously where dramatic ECSA loss is observed within the first 500 cycles. This is a pure particle size effect that more or less behaves similar to the inverse function 1/x in which surface area of spherical particle per gram is plotted against particle diameter. Decrease in ECSA is generally accounted for growing in particle catalyst due to cluster migration and coalescence (ripening), catalyst dissolution as well as support corrosion. After ADT procedure, amount of ECSA retention of thermal treated catalysts is about 17% higher than that of as-prepared one for both systems (see Fig. 4c). It can be concluded that Pt particles size as well as nature of carbon support included anchored functional groups may play a preponderant role with respect to catalyst stability. Surprisingly, after 500 ADT cycles, ECSA of Pt/HGS_{850 °C} is about 20% higher than that measured at beginning

of the experiment and highly reproducible results were recorded that are in very good agreement with other literature sources [38,43,44]. This is attributed to oxidative removal of residual carbon or/and organic species from synthesis that may poison/block platinum surface. Interestingly, after temperature treatment at 850 °C, degradation rate of both systems behaves more or less linear and parallel.

3.4. Microscopic investigation of GDE surface and thickness

Microscopic investigation of the as-prepared GDE surface area and thickness were performed by SEM technique. On the first row in Fig. 5a, surface topography of as-received microporous layer (MPL) is shown at different magnifications. One can recognize a bimodal pore matrix made of smaller (<500 nm) and larger (1–3 μm) ones for gas and water transport, respectively. Quality of the reaction layer coated MPL after sintering step depends on different parameters such as water/solvent content, heating rate and intrinsic

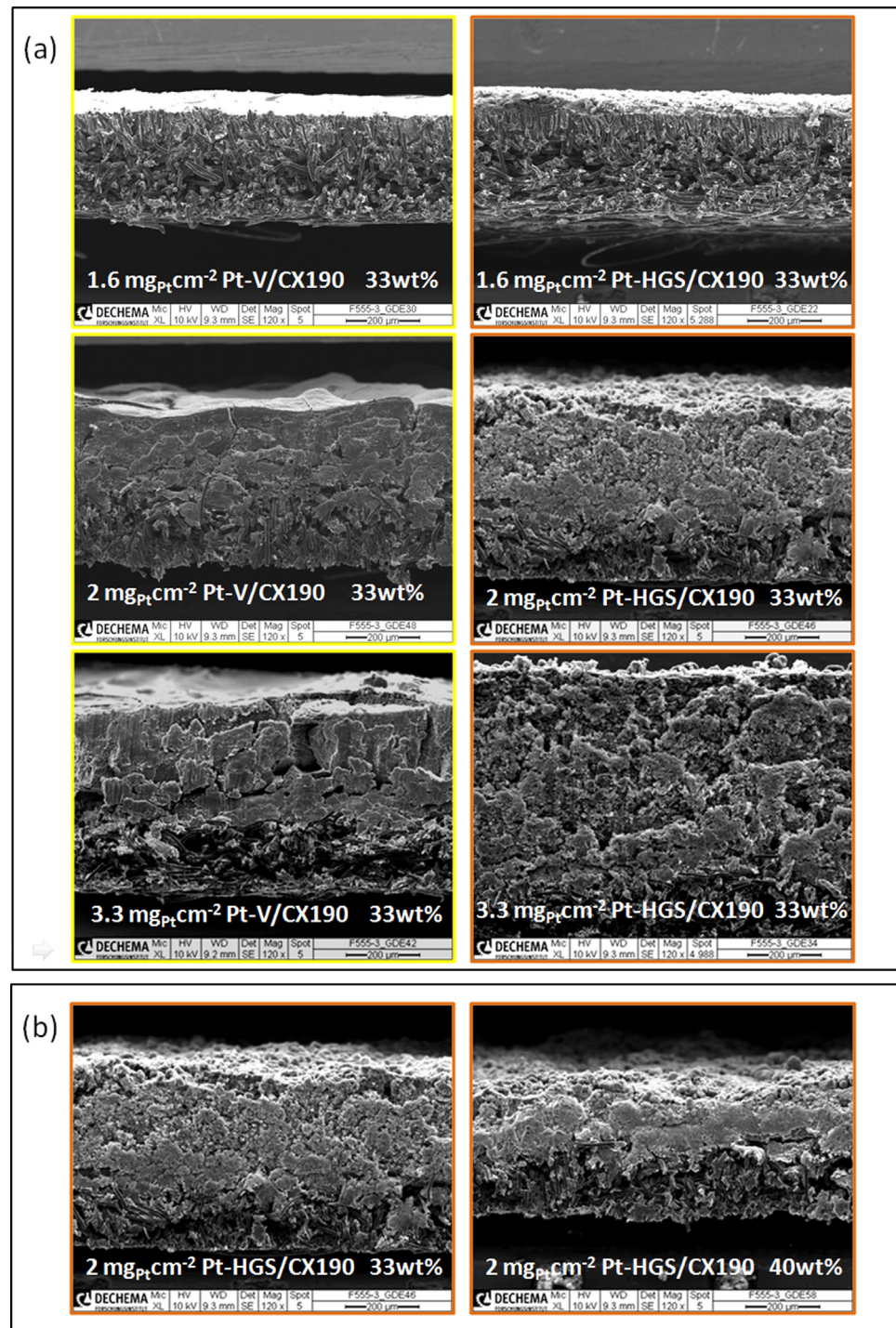


Fig. 6. SEM images of cross-sectioned GDEs cathodes with (a) 33 wt% Pt on Vulcan & HGS at different Pt loading and (b) 33 and 40 wt% Pt on HGS support at $2 \text{ mg}_{\text{Pt}} \text{cm}^{-2}$.

properties of active materials, such as hydrophobic/hydrophilic properties but also on dispersion ability in the solvent. SEM images of cathode surfaces are presented on Fig. 5b and c. Surface of Vulcan-based electrode is relatively smooth (Fig. 5b) but affected by large cracks created during solvent evaporation step. No obvious correlation between layer thickness and cracks density/width was concluded. It is also not clear, whether cracks may have a positive influence e.g. water transport at high current densities. By contrast, numerous agglomerates are visible on Pt/HGS electrode surface that may affect quality of electrode/membrane interface.

In Fig. 6, SEM images of cross-sectioned GDEs are presented. It should be noted that as-prepared GDE have been simply cut with scissors and did not undergone any compression stress before as under fuel cell conditions. Layer thickness of the GDEs with HGS support varies from 160 to 580 μm as catalyst loading increased from of 1.6 to 3.3 $\text{mg}_{\text{Pt}} \text{cm}^{-2}$. In comparison, layer thickness of Vulcan-based GDEs increased from 120 to 360 μm . Difference in layer thickness between HGS and Vulcan support amounts 40 and 220 μm for smallest and largest catalyst loading, respectively. Large difference in layer thickness, especially at high loading, between both systems results obviously from dead volume of both inner hol-

Table 2

Summary of the contents and the maximal power densities of different MEAs.

MEAs cathode catalyst system	Pt loading (concentration) $\text{mg}_{\text{Pt}} \text{cm}^{-2}$		$P_{\text{max}} \text{mW cm}^{-2}$ at $110^{\circ}\text{C}, 2 \text{bar}$		RL cathode thickness μm
	anode	cathode	oxygen	air	
MEA1: Pt/HGS	2 (37.5 wt%)	1.6 (33 wt%)	223	110	160
MEA2: Pt/Vulcan	2 (37.5 wt%)	1.6 (33 wt%)	200	105	120
MEA3: Pt/HGS	2 (37.5 wt%)	2 (33 wt%)	200	110	360
MEA4: Pt/Vulcan	2 (37.5 wt%)	2 (33 wt%)	220	120	264
MEA5: Pt/HGS	2 (37.5 wt%)	3.3 (33 wt%)	160	100	580
MEA6: Pt/Vulcan	2 (37.5 wt%)	3.3 (33 wt%)	250	179	360
MEA7: Pt/HGS 850°C	2 ^a (50 wt%)	2 (40 wt%)	310	160	200
MEA8: Pt/Vulcan	2 ^a (50 wt%)	2 (33 wt%)	240	80	264

^a PtRu-HISPEC 12100 was used as anode catalyst.

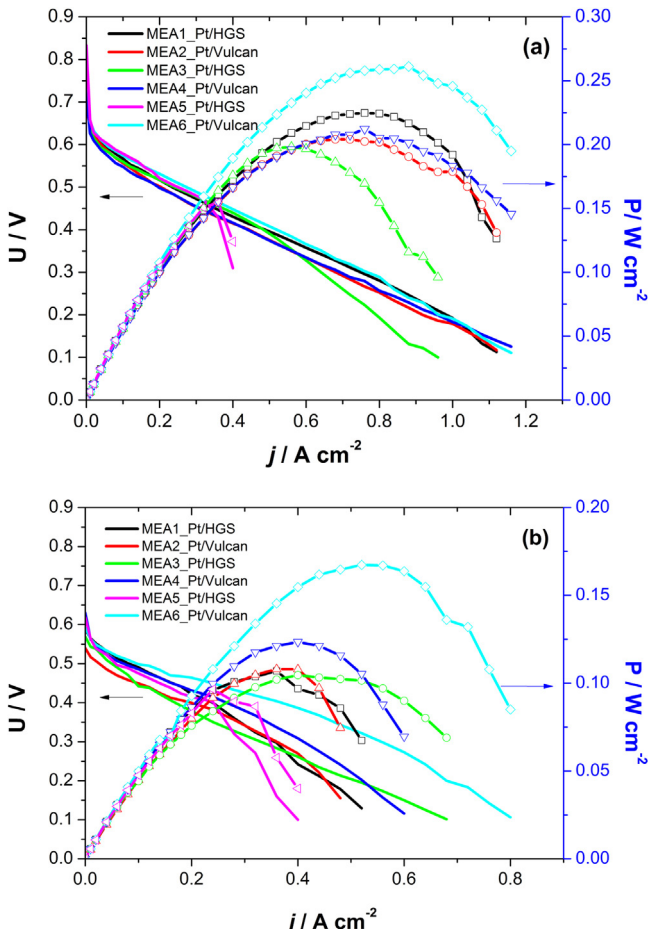


Fig. 7. Influence of catalyst loading and carbon nature at the cathode on cell power performance (a) in pure oxygen and (b) in air at 110°C and 2 bar.

low spheres and space between them since the larger the diameter sphere (340 nm for HGS vs. 50 nm for Vulcan) the higher the porosity. After increasing Pt concentration from 33 up to 40 wt%, however, layer thickness of $2 \text{ mg}_{\text{Pt}} \text{cm}^{-2}/\text{HGS}$ became significantly thinner (Fig. 6b). Most relevant values are summarized in Table 2.

3.5. Polarization experiments

3.5.1. Influence of catalyst loading on cell performance

Influence of catalyst loading and nature of the carbon used in the cathode catalyst layer on power density at 110°C is presented in Fig. 7. At $1.6 \text{ mg}_{\text{Pt}} \text{cm}^{-2}$ catalyst loading, MEA1 with Pt-HGS as cathode material shows higher performances than those of MEA2 with Pt-Vulcan. Hereby, a maximum cell power density of 223 mW cm^{-2} was measured in oxygen and air, respectively. At

higher current density and catalyst loading, however, influence of mass transport limitation in HGS-containing MEA3 & 5 has become evident, especially during measurements in air. Hereby, MEA with Vulcan-based cathode material shows obviously better performance that culminates at about 179 mW cm^{-2} with $3.3 \text{ mg}_{\text{Pt}} \text{cm}^{-2}$. For DMFC application where catalyst loading of at least $2 \text{ mg}_{\text{Pt}} \text{cm}^{-2}$ is usually required to yield acceptable power densities, diameter of carbon spheres should preferentially lay in the range of 50–100 nm in order to reduce dead volume, electrode thickness and as a consequence mass transport contribution.

3.5.2. Influence of cathodic catalyst concentration and working temperature on HGS-based MEA performance

In order to increase catalyst accessibility and decrease reaction layer thickness, Pt/HGS catalyst was previously subjected to a temperature treatment in N_2 at 850°C and its Pt concentration was increased up to 40%, respectively. Additionally, as-prepared 37.5 wt% PtRu was replaced by a commercial 50 wt% one. For this novel MEA7, the practice-relevant loading of $2 \text{ mg}_{\text{Pt}} \text{cm}^{-2}$ at both anode and cathode was chosen. Afterwards, performance of HGS-based cell at 80°C jumps from 200 to 235 mW cm^{-2} in oxygen and from 105 to 135 mW cm^{-2} in air feed (see Fig. 8). Moreover, positive effect of elevated cell temperature on maximal cell power density was achieved. At 110°C and 2 bar, maximal power density of MEA7 amounted 310 mW cm^{-2} with oxygen and 155 mW cm^{-2} with air. In the Nyquist plot shown in Fig. 8e and 8f, ohmic resistance value R_E was about $250 \text{ m}\Omega \text{cm}^2$ for HGS-based MEA compared to about $500 \text{ m}\Omega \text{cm}^2$ for Vulcan-based MEA. It is obvious that incorporation of HGS as catalyst support has a beneficial effect on GDE ohmic resistance. That can be explained by both higher conductivity of graphitic-rich domains and presumably less contact resistance between the quite large HGS particles compared to that of smaller amorphous Vulcan ones. Temperature dependency of EIS response is more pronounced in case of MEA8. Overall charge transfer resistance R_{CT} of both systems was evaluated by adding half-circle contributions according to arrowed area drawn in Fig. 8e, where small half-circle is related to cathodic and larger one to anodic charge transfer resistance. Distinction of respective contributions has been demonstrated by feeding DMFC cathode with hydrogen and mathematically subtracting values obtained during experiments in air by those in hydrogen [45]. One can observe a slightly positive influence of the applied temperature on performance of HGS-based MEA because anodic mass transfer-induced half-circle is getting smaller with increasing temperature. In Fig. 8f, it can be seen that increase in cell temperature from 80 to 100°C leads to a R_E shift from 450 up to $525 \text{ m}\Omega \text{cm}^2$, respectively. This is obviously due to perturbation in water alimentation of polymer membrane at elevated temperature that is more or less compensated by enhanced electrode kinetics reactions at least until 90°C . At 100°C , however, shape of impedance plots was not reproducible, which is an indication for disturbed cell functionality probably due to local depletion in ionomer water content. Although no Warburg behavior was

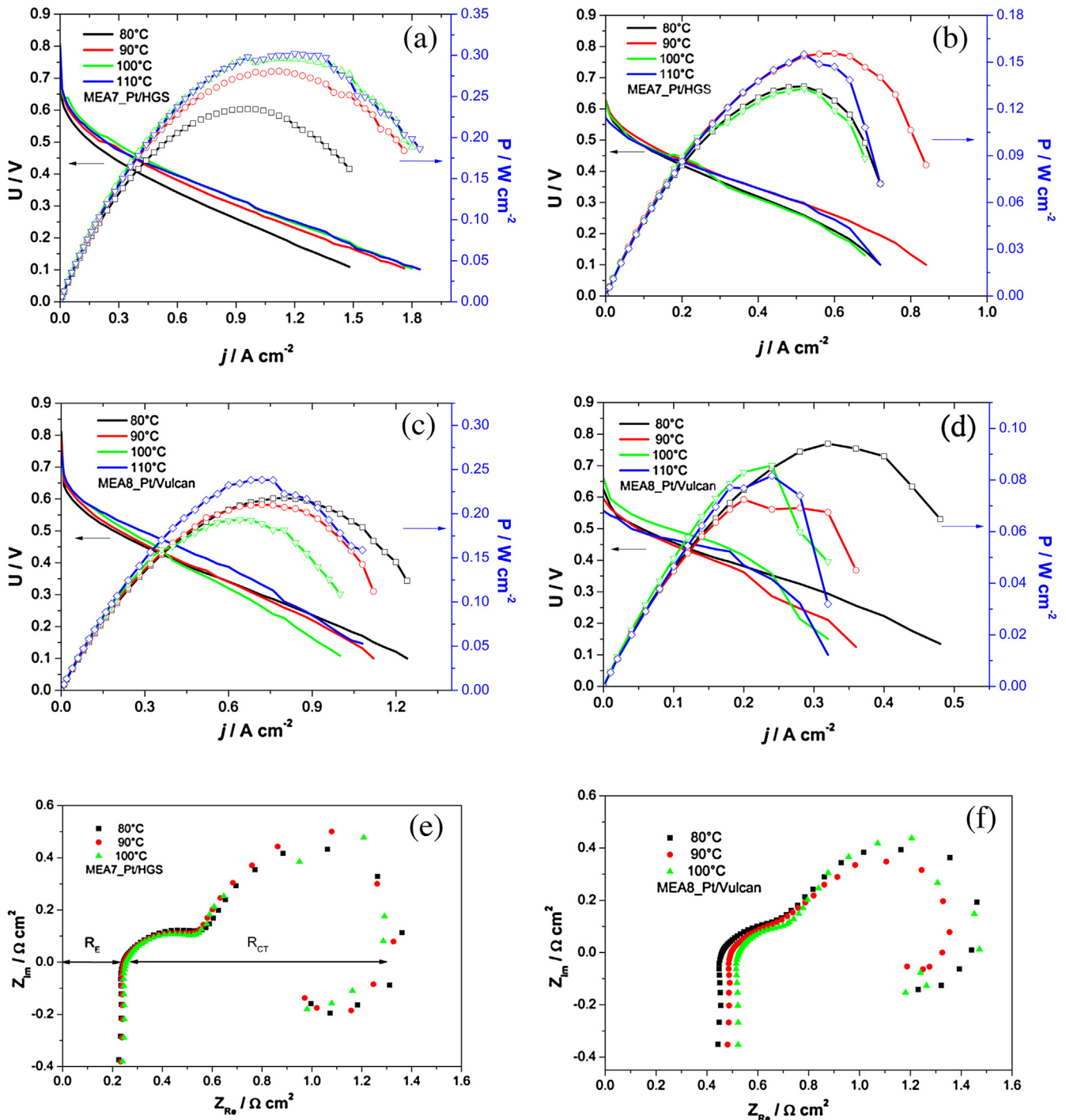


Fig. 8. Influence of cell temperature on (a and b) HGS-based and (c & d) Vulcan-based MEA performance either in (a and c) oxygen or in (b and d) air at 2 bar. (e and f) Niquyist plot of both MEAs at different temperatures in oxygen at OCV and 2 bar.

detected, effect of episodic changes in mass transfer resistance cannot be definitively excluded since some impedance values spread far outside optimal semi-circle trajectory (values not shown here).

For better clarity, maximal power density values as function of the catalyst support and catalyst loading are summarized in Table 2.

3.6. SEM images and WDX spectra of cross-sectioned MEAs

Evaluation of the layer quality and element distribution was made by SEM and WDX (Wavelength Dispersive X-ray analysis), respectively at cross-sectioned MEAs after test in laboratory cell.

SEM/EDX investigations focus more specially on cathode composition in terms of absolute Pt concentration whereas WDX analysis aims to determine spatial distribution of single elements such as fluorine, carbon and platinum in the HGS-based cathode. While Pt-Vulcan-based cathode remained homogenous (Fig. 9a), large agglomerates in Pt/HGS-based reaction layer are visible in Fig. 9b and 9c that presumably results from inhomogeneous Pt/HGS suspension during ink preparation and/or coating step. Surprisingly, EDX analysis didn't reveal any excessive Pt concentration gradient within HGS-based reaction layer area. Within the dark grey area delimited by the small red square in Fig. 9c, Pt concentration

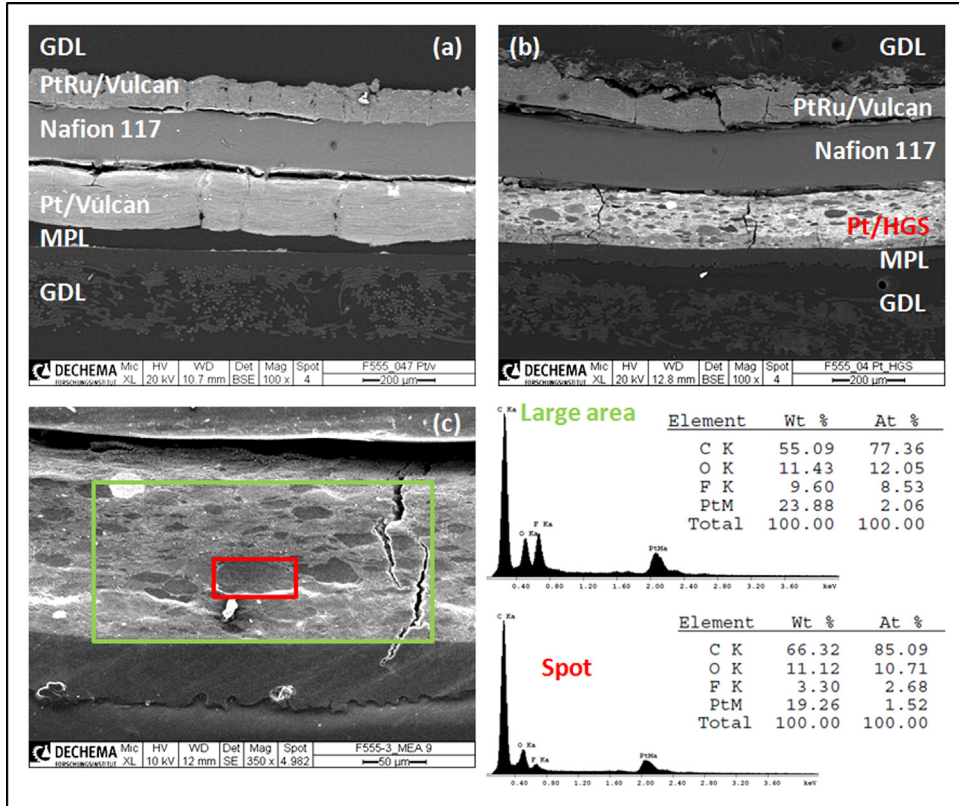


Fig. 9. SEM-images of post-mortem cross-sectioned MEAs with (a) Pt/Vulcan- and (b) Pt/HGS-based cathode after operation in DMFC as well as (c) corresponding EDX spectra.

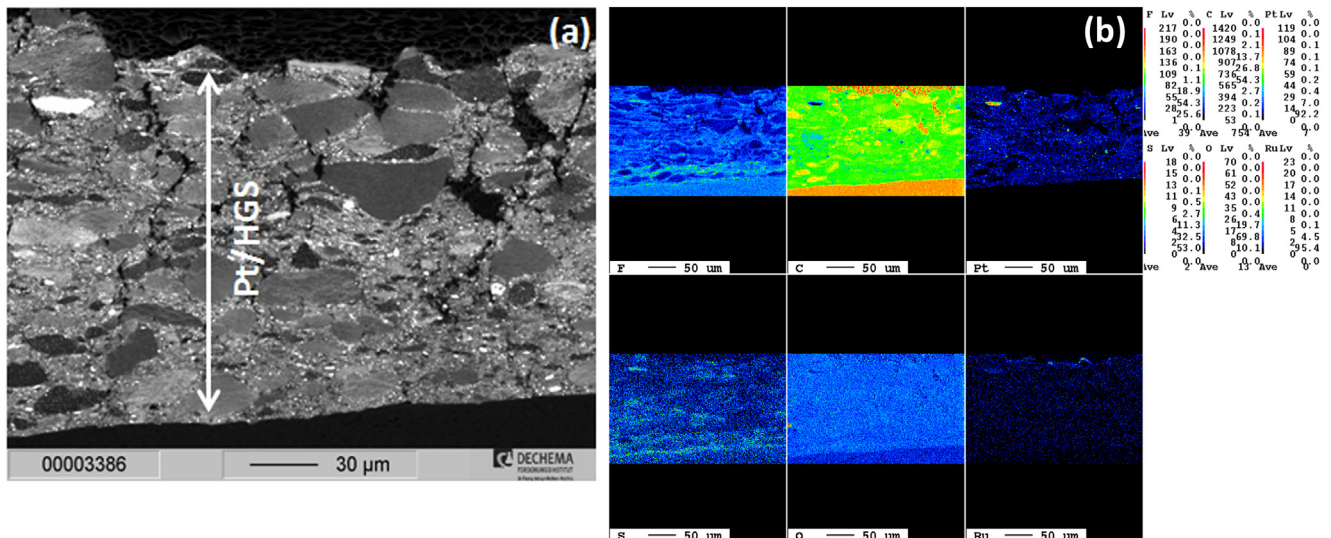


Fig. 10. (a) SEM image of selected area in HGS cathode. (b) WDX spectra of the element concentrations on a μm-scale illustrated by using a colour palette from dark blue (low) to red (high). (Colored mapping patterns are only visible in pdf version.)

amounts 19.3 wt% compared to 23.9 wt% in the large green square. It appears that MEA investigations led to a depletion of Pt concentration of about 10 wt% compared to the as-prepared electrodes. Fig. 10 shows SEM and WDX elemental mapping of a portion of a Pt/HGS-based cathode. The bright spots in Fig. 10a are clearly related to Pt-rich domains while darker spots to carbon-rich ones. We believe that the emergence of dark/bright contrast regions is related to randomly distribution of the inner/outer surface of cross-sectioned carbon hollow spheres that have been created during

sample cutting/polishing. There is no evidence of crossed over Ru on the cathode.

Interestingly, a quite similar layer thickness of 200 μm has been estimated for both 3.3 mg_{Pt} cm⁻² on Vulcan- and HGS-based reaction layers that must have undergone an impressive shrinkage of 160 and 360 μm, respectively during compression step of respective MEA at 7 bar (see layer thickness values after coating step in Table 2). This should have somehow led to partial collapse of most

fragile hollow spheres and as a consequence hinder proper mass transport of educts and products within Pt/HGS layer.

4. Conclusion

In this work, influence of cathodic catalyst support and loading on performance of a middle-temperature DMFC was studied. First, ADT procedure was applied to 33 wt% Pt/Vulcan and Pt/HGS in 1 M H₂SO₄ under half-cell condition. ECSA loss was more pronounced in case of Vulcan-supported catalyst. After temperature treatment at 850 °C, improvement in ECSA retention was observed at both systems. Despite intensive ultrasonic step to properly disperse HGS powder in ink suspension, numerous agglomerates were visible on SEM images of electrode surface and cross-section. At catalyst loading close to 1.5 mg_{Pt} cm⁻², MEA with high graphitized hollow spheres exhibited best performances compared to MEA with Vulcan-supported cathode. At higher catalyst loading, however, reverse trend was observed. This was attributed to mass transport limitation in HGS-based reaction layer. Beneficial effect of temperature treatment at 850 °C and mesoporous hosting structure on Pt catalyst longevity has been clearly demonstrated. Dense catalyst concentration up to 50 and 40 wt% in anode and cathode reaction layer, respectively also improved overall MEA performance. This was attributed to diminution in electrode thickness and consequently to shorter transport distances for educts and products. Ideally, diameter of catalyst support should not exceed 50–100 nm.

Acknowledgments

The authors gratefully thank Dr. C. Galeano and Prof. F. Schüth from Max-Planck institute for carbon research in Mülheim an der Ruhr for HGS material synthesis, TGA analysis and valuable discussions. We thank Dr. G. Schmidt for EPMA analysis. “Deutsche Forschungsgemeinschaft” (DFG) (DR 812/1-1) and “Bundesministerium für Wirtschaft und Energie” (BMWi) (16593 BG & 16594 N1) are acknowledged for financial support.

Appendix A. Supplementary data

Supplementary data associated with this article can be found, in the online version, at <http://dx.doi.org/10.1016/j.apcatb.2016.11.014>.

References

- [1] N. Armaroli, V. Balzani, The future of energy supply: challenges and opportunities, *Angew. Chem.* 46 (2006) 52–66.
- [2] N.S. Lewis, D.G. Nocera, Powering the planet chemical challenges in solar energy utilization, *Proc. Natl. Acad. Sci. U. S. A.* 103 (2006) 15729–15735.
- [3] The Toyota Mirai car powered by hydrogen fuel cell, <https://ssl.toyota.com/mirai/fcv> (accessed 09.09.16).
- [4] P. Costamagna, S. Srinivasan, Quantum jumps in the PEMFC science and technology from the 1960 to the year 2000 part I. Fundamental scientific aspects, *J. Power Sources* 102 (2001) 242–252.
- [5] M.L. Perry, T.F. Fuller, A historical perspective of fuel cell technology in the 20th century, *J. Electrochem. Soc.* 149 (2002) S59–S67.
- [6] S. Sharma, B.G. Pollet, Support materials for PEMFC and DMFC electrocatalysts—a review, *J. Power Sources* 208 (2012) 96–119.
- [7] V. Neburchilov, J. Martin, H. Wang, J. Zhang, A review of polymer electrolyte membranes for direct methanol fuel cells, *J. Power Sources* 169 (2007) 221–238.
- [8] N. Bogolowski, B. Iwanschitz, J.-F. Drillet, Development of a coking-resistant NiSn anode for the direct methane SOFC, *Fuel Cells* 15 (2015) 711–717.
- [9] X.-Z. Yuan, H. Wang, PEM fuel cell fundamentals, in: J. Zhang (Ed.), *PEM Fuel Cell Electrocatalysts and Catalyst Layers: Fundamentals and Applications*, Springer, London, 2008, pp. 1–79.
- [10] A. Arvay, E. Yli-Rantala, C.-H. Liu, X.-H. Peng, P. Koski, L. Cindrella, P. Kauranen, P.M. Wilde, A.M. Kannan, Characterization techniques for gas diffusion layers for proton exchange membrane fuel cells—a review, *J. Power Sources* 213 (2012) 317–333.
- [11] E.J. See, S.G. Kandlikar, Effect of GDL material on thermal gradients along the reactant flow channels in PEMFCs, *ECS Trans.* 58 (2013) 867–880.
- [12] S. Park, J.-W. Lee, B.N. Popov, A review of gas diffusion layer in PEM fuel cells: materials and designs, *Int. J. Hydrogen Energy* 37 (2012) 5850–5865.
- [13] H. Li, K. Lee, J. Zhang, Electrocatalytic H₂ oxidation reaction, in: J. Zhang (Ed.), *PEM Fuel Cell Electrocatalysts and Catalyst Layers*, Springer, London, 2008, pp. 135–159.
- [14] F. Hasché, M. Oezaslan, P. Strasser, Activity, stability, and degradation mechanisms of dealloyed PtCu₃ and PtCo₃ nanoparticle fuel cell catalysts, *ChemCatChem* 3 (2011) 1805–1813.
- [15] F. Hasché, M. Oezaslan, P. Strasser, Activity, structure and degradation of dealloyed PtNi₃ nanoparticle electrocatalyst for the oxygen reduction reaction in PEMFC, *J. Electrochem. Soc.* 159 (2012) B24–B33.
- [16] P. Strasser, S. Koh, T. Anniyev, J. Greeley, K. More, C. Yu, Z. Liu, S. Kaya, D. Nordlund, H. Ogasawara, M.F. Toney, A. Nilsson, Lattice-strain control of the activity in dealloyed core–shell fuel cell catalysts, *Nat. Chem.* 2 (2010) 454–460.
- [17] P.W. Atkins, *Physical Chemistry*, third ed., W.H. Freeman and Company, New York, 1986.
- [18] M.W. Chase, *NIST-JANAF Thermochemical Tables*, fourth ed., American Chemical Society and the American Institute of Physics for the National Bureau of Standards, New York, 1998.
- [19] S.W. Angrist, *Direct Energy Conversion*, second ed., Allyn and Bacon Boston, 1971.
- [20] N. Bogolowski, J.-F. Drillet, Appropriate balance between methanol yield and power density in portable direct methanol fuel cell, *Chem. Eng. J.* 270 (2015) 91–100.
- [21] S. Song, K. Wang, Y. Liu, C. He, Y. Liang, R. Fu, D. Wu, Y. Wang, Highly ordered mesoporous carbons as the support for Pt catalysts towards alcohol electrooxidation: the combined effect of pore size and electrical conductivity, *Int. J. Hydrogen Energy* 38 (2013) 1405–1412.
- [22] K. Wang, Y. Wang, Z. Liang, Y. Liang, D. Wu, S. Song, P. Tsiaikaras, Ordered mesoporous tungsten carbide/carbon composites promoted Pt catalyst with high activity and stability for methanol electrooxidation, *Appl. Catal. B* 147 (2014) 518–525.
- [23] R. Ryoo, S.H. Joo, M. Kruk, M. Jaroniec, Ordered mesoporous carbons, *Adv. Mater.* 13 (2001) 677–681.
- [24] G. Zhao, J. He, C. Zhang, J. Zhou, X. Chen, T. Wang, Highly dispersed Pt nanoparticles on mesoporous carbon nanofibers prepared by two templates, *J. Phys. Chem. C* 112 (2008) 1028–1033.
- [25] J. Ding, K.Y. Chan, J. Ren, F. Xiao, Platinum and platinum–ruthenium nanoparticles supported on ordered mesoporous carbon and their electrocatalytic performance for fuel cell reactions, *Electrochim. Acta* 50 (2005) 3131–3141.
- [26] F. Su, J. Zeng, X. Bao, Y. Yu, J.Y. Lee, X.S. Zhao, Preparation and characterization of highly ordered graphitic mesoporous carbon as a Pt catalyst support for direct methanol fuel cells, *Chem. Mater.* 17 (2005) 3960–3967.
- [27] S.H. Joo, C. Pak, D.J. You, S.A. Lee, H.I. Lee, J.M. Kim, H. Chang, D. Seung, Ordered mesoporous carbons (OMC) as supports of electrocatalysts for direct methanol fuel cells (DMFC): effect of carbon precursors of OMC on DMFC performances, *Electrochim. Acta* 52 (2006) 1618–1626.
- [28] H. Chang, S.H. Joo, C. Pak, Synthesis and characterization of mesoporous carbon for fuel cell, *J. Mater. Chem.* 17 (2007) 3078–3088.
- [29] S. Song, Y. Liang, Z. Li, Y. Wang, R. Fu, D. Wu, P. Tsiaikaras, Effect of pore morphology of mesoporous carbons on the electrocatalytic activity of Pt nanoparticles for fuel cell reactions, *Appl. Catal. B* 98 (2010) 132–137.
- [30] J.R.C. Salgado, F. Alcaide, G. Álvarez, L. Calvillo, M.J. Lázaro, E. Pastor, Pt–Ru electrocatalysts supported on ordered mesoporous carbon for direct methanol fuel cell, *J. Power Sources* 195 (2010) 4022–4029.
- [31] B. Liu, S. Creager, Silica-sol-templated mesoporous carbon as catalyst support for polymer electrolyte membrane fuel cell applications, *Electrochim. Acta* 55 (2010) 2721–2726.
- [32] L. Calvillo, M. Gangeri, S. Perathoner, G. Centi, R. Moliner, M.J. Lázaro, Synthesis and performance of platinum supported on ordered mesoporous carbons as catalyst for PEM fuel cells: effect of the surface chemistry of the support, *Int. J. Hydrogen Energy* 36 (2011) 9805–9814.
- [33] M.L. Lin, M.Y. Lo, C.Y. Mou, PtRu nanoparticles supported on ozone-treated mesoporous carbon thin film as highly active anode materials for direct methanol fuel cells, *J. Phys. Chem. C* 113 (2009) 16158–16168.
- [34] X. Cui, J. Shi, L. Zhang, M. Ruan, J. Gao, PtCo supported on ordered mesoporous carbon as an electrode catalyst for methanol oxidation, *Carbon* 47 (2009) 186–194.
- [35] S.H. Joo, H.I. Lee, D.J. You, K. Kwon, J.H. Kim, Y.S. Choi, M. Kang, J.M. Kim, C. Pak, H. Chang, D. Seung, Ordered mesoporous carbons with controlled particle sizes as catalyst supports for direct methanol fuel cell cathodes, *Carbon* 46 (2008) 2034–2045.
- [36] S.H. Liu, C.C. Chiang, M.T. Wu, S.B. Liu, Electrochemical activity and durability of platinum nanoparticles supported on ordered mesoporous carbons for oxygen reduction reaction, *Int. J. Hydrogen Energy* 35 (2010) 8149–8154.
- [37] R. Liu, D. Wu, X. Feng, K. Müllen, Nitrogen-doped ordered mesoporous graphitic arrays with high electrocatalytic activity for oxygen reduction, *Angew. Chem. Int. Ed.* 49 (2010) 2565–2569.
- [38] C. Galeano, J.C. Meier, V. Peinecke, H. Bongard, I. Katsounaros, A.A. Topalov, A. Lu, K.J.J. Mayrhofer, F. Schüth, Toward highly stable electrocatalysts via nanoparticle pore confinement, *J. Am. Chem. Soc.* 134 (2012) 20457–20465.
- [39] A.L. Patterson, The Scherrer formula for X-ray particle size determination, *Phys. Rev.* 56 (1939) 978–981.

[40] A. Guha, W. Lub, T.A. Zawodzinski, D.A. Schiraldia, Surface-modified carbons as platinum catalyst support for PEM fuel cells, *Carbon* 45 (2007) 1506–1517.

[41] A. Grondein, D. Bélanger, Covalent grafting of aminated compounds on Vulcan XC72R by melamine in situ diazotization, *Carbon* 50 (2012) 4335–4342.

[42] R.T.K. Baker, The relationship between particle motion on a graphite surface and Tamman temperature, *J. Catal.* 78 (1982) 473–476.

[43] S. Mezzavilla, C. Baldizzone, K.J.J. Mayrhofer, F. Schüth, General method for the synthesis of hollow mesoporous carbon spheres with tunable textural properties, *ACS Appl. Mater. Interfaces* 7 (2015) 12914–12922.

[44] C. Galeano, J.C. Meier, M. Soorholtz, H. Bongard, C. Baldizzone, K.J.J. Mayrhofer, F. Schüth, Nitrogen-doped hollow carbon spheres as a support for platinum-based electrocatalysts, *ACS Catal.* 4 (2014) 3856–3868.

[45] J.-F. Drillet, Einsatz von poly(3,4-ethylenedioxythiophen) als katalysatorträger und methanolbarriere in der anode der direktmethanol-brennstoffzelle, Ph.D. Thesis, Shaker Verlag Aachen, 2009.